



# Delayed formation of coherence in the emission dynamics of high-Q nanolasers

GALAN MOODY,<sup>1,\*</sup> MAWUSSEY SEGNON,<sup>2</sup> ISABELLE SAGNES,<sup>3</sup> RÉMY BRAIVE,<sup>3,4</sup> ALEXIOS BEVERATOS,<sup>3</sup> ISABELLE ROBERT-PHILIP,<sup>3</sup> NADIA BELABAS,<sup>3</sup> FRANK JAHNKE,<sup>2</sup> KEVIN L. SILVERMAN,<sup>1</sup> RICHARD P. MIRIN,<sup>1</sup> MARTIN J. STEVENS,<sup>1</sup> AND CHRISTOPHER GIES<sup>2</sup>

<sup>1</sup>National Institute of Standards and Technology, 325 Broadway, Boulder, Colorado 80305, USA

<sup>2</sup>Institute for Theoretical Physics, University of Bremen, 28334 Bremen, Germany

<sup>3</sup>Centre de Nanosciences et de Nanotechnologies, CNRS, Univ. Paris Sud, Université Paris-Saclay, C2N Marcoussis, 91460 Marcoussis, France

<sup>4</sup>Université Paris Diderot, Sorbonne Paris Cité, 75207 Paris cedex 13, France

\*Corresponding author: galan.moody@nist.gov

Received 13 December 2017; revised 12 February 2018; accepted 21 February 2018 (Doc. ID 315717); published 30 March 2018

**In the realization of ultrasmall semiconductor lasers, cavity-QED effects are used to enhance spontaneous emission and enable the lasing threshold to be crossed with gain contributions from only a few solid-state emitters. Operation in this regime fosters correlation effects that leave their fingerprint especially in the emission dynamics of nanolasers. Using time-resolved photon-correlation spectroscopy, we show that in a quantum-dot photonic-crystal nanolaser emitting in the telecom band, second-order coherence associated with lasing is established on a different timescale than the emission itself. By combining measurements with a microscopic semiconductor laser theory, we attribute the origin to carrier-photon correlations that give rise to non-Markovian effects in the emission dynamics that are not captured by laser rate-equation theories. Our results have direct implications with respect to the modulation response, repetition rate, noise characteristics, and coherence properties of nanolasers for device applications.** © 2018 Optical Society of America under the terms of the [OSA Open Access Publishing Agreement](#)

**OCIS codes:** (350.4238) Nanophotonics and photonic crystals; (140.5960) Semiconductor lasers; (030.5290) Photon statistics; (030.1640) Coherence; (230.5590) Quantum-well, -wire and -dot devices.

<https://doi.org/10.1364/OPTICA.5.000395>

## 1. INTRODUCTION

The quest for miniaturization of integrable and energy-efficient optoelectronic devices has led to the development of semiconductor nanolasers with increasingly smaller footprints and nearly thresholdless operation [1]. Optical microcavities are used to confine the electromagnetic field to the extent of the wavelength, including photonic-crystal (PhC) cavities that combine a small mode volume with a long photon storage time. The small mode volume places a limit on the amount of gain material that can be brought into spatial overlap with the mode. To acquire sufficient gain to sustain lasing, spontaneous emission is enhanced via the Purcell effect [2,3], pushing the concept of lasing into a cavity-QED regime governed by photonic and electronic correlation and fluctuation effects [4–9].

The influence of correlations on lasing is not easily revealed, but it most often manifests in the dynamical properties of the emission, especially following a short excitation pulse. Here, we show that in a semiconductor nanolaser, carrier-photon correlations—enhanced by cavity-QED effects—lead to a breakdown of the traditional lasing picture in which coherent emission is directly related to the presence of stimulated emission. Using a modified Hanbury Brown and Twiss (HBT) experimental

setup, we measure the time-resolved emission dynamics of a quantum-dot (QD) PhC nanolaser, which provides a complete two-time map of the second-order intensity correlation function,

$$g^{(2)}(t_1, t_2) = \frac{\langle b^\dagger(t_1)b^\dagger(t_2)b(t_2)b(t_1) \rangle}{\langle b^\dagger(t_1)b(t_1) \rangle \langle b^\dagger(t_2)b(t_2) \rangle}, \quad (1)$$

where  $b^\dagger$  and  $b$  are the respective photon creation and annihilation operators of the optical mode of interest and  $t_1$  and  $t_2$  are the photon detection times. The full dynamics of  $g^{(2)}(t_1, t_2)$  provide insight into the buildup of coherence due to the onset of stimulated emission after the lasing threshold has been crossed. “Coherent” here simply means that the second-order correlation function has the same value it would for coherent state emission:  $g^{(2)}(t_1, t_1) = 1$ . In this case, the variance in the photon number is equal to that of a coherent state with the same mean photon number. Although  $g^{(2)}(t_1, t_1) = 2$  for an ideal thermal source, here we use “thermal” to refer to any case where  $g^{(2)}(t_1, t_1) > 1$ . In this notation, thermal emission simply implies a larger variance in photon number than for a coherent state. Unexpectedly, we observe that coherent emission is not fully reached at the maximum intensity of the emitted pulse. Instead, it is delayed by up to

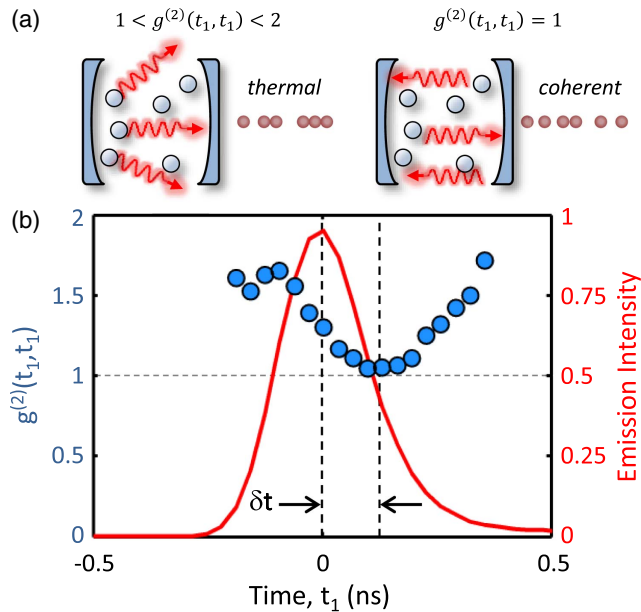


**Fig. 1.** (a) For a nanolaser operating below the threshold, spontaneous emission into the cavity mode leads to thermal radiation with  $g^{(2)}(t_1, t_1) > 1$ . Above the threshold, the onset of stimulated emission leads to coherent radiation with  $g^{(2)}(t_1, t_1) = 1$ . (b) In a cavity-QED QD nanolaser, in which only a few emitting dipoles are coupled to a high cavity-quality-factor mode, the transition from thermal to coherent radiation (points) is delayed by  $\delta t$  with respect to the emission pulse maximum (solid line). This delay arises from non-Markovian effects in the dynamics of carrier-photon correlations.

250 ps so that the emission has a large thermal component above the lasing threshold, as shown in Fig. 1.

The experimental results are confirmed by microscopic calculations of the output intensity and photon autocorrelation function. In the theory, both quantities obey different dynamical equations. At the lasing threshold, the dynamics of the output intensity are primarily determined by stimulated emission, while  $g^{(2)}(t_1, t_2)$  follows carrier-photon correlations that are analogous to stimulated emission but in the presence of an additional photon. Here, we show that the individual time dynamics of these higher-order correlations determining  $g^{(2)}(t_1, t_2)$ , but not the emission intensity, are responsible for the delay in coherent emission in a non-Markovian manner. This effect is facilitated by the combination of a high cavity-quality factor  $Q$  and a small amount of gain provided by a few solid-state emitters in the PhC nanocavity.

In Section 2, we characterize our PhC laser with a temperature-tunable gain and show input-output curves in the light-emitting diode (LED) and lasing operational regimes. In Section 3, the microscopic laser model that provides access to the laser and photon-correlation dynamics is introduced. Maps of the two-time autocorrelation function are presented in Section 4. The two-time diagonal provides the zero-delay photon autocorrelation function, which reveals the novel effect of delayed coherence formation presented in Section 5.

## 2. NANOLASER CHARACTERISTICS

### A. Sample Characterization and Temperature Tuning of the Emitter Number

The nanolaser gain material comprises a single layer of InAsP QDs at the center of a 320 nm thick InP layer grown by metal

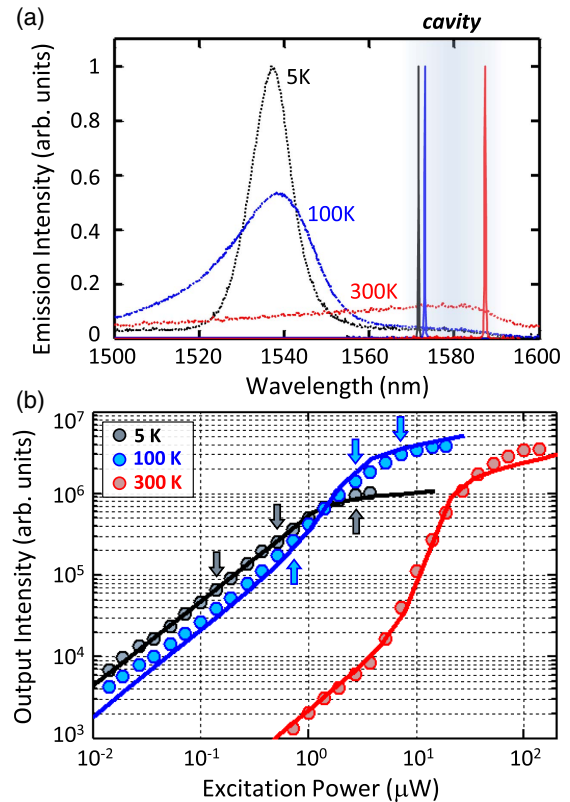


**Fig. 2.** (a) InAsP/InP QD spontaneous emission and cavity mode emission for three different temperatures. Measurements of the cavity linewidth at all temperatures are limited by the spectrometer resolution, placing a lower bound on the cavity quality-factor  $Q > 50,000$ . (b) Nanolaser output intensity versus input optical power for nonresonant pulsed excitation at three different temperatures, demonstrating the transition from the LED regime (5 K) to stimulated emission (300 K). The light-in/light-out curves are reproduced by the microscopic laser theory (solid lines). The arrows denote the excitation powers  $P_1$ ,  $P_2$ , and  $P_3$  for the data shown in Fig. 5.

organic vapor phase epitaxy [10,11]. The QD density is on the order of  $10^{10} \text{ cm}^{-2}$ . A hexagonal PhC structure with a lattice constant of  $a_m = 410 \text{ nm}$  and an air-hole radius of  $r = 0.293a_m$  is fabricated using electron-beam lithography, a plasma-etching process to form the PhC, and wet etching to suspend the InP membrane. A high- $Q$  cavity is formed from three missing holes ( $L_3$ -type defect cavity), yielding a nanocavity with an effective mode volume of  $1.3(\lambda/n)^3$  containing on the order of few tens of QDs. The position of the two holes forming the end mirrors of the cavity have been displaced outward by  $0.18a_m$  to enhance the cavity  $Q$ . Measurements of the cavity linewidth, shown in Fig. 2(a), yield  $\gamma_c = 0.03 \text{ nm}$ , which is the resolution limit of the spectrometer. While this places a lower bound of 50,000 on the  $Q$  factor at all temperatures, from our theoretical analysis we estimate a value that is approximately three times higher, corresponding to a cavity lifetime of  $\tau_c = 230 \text{ ps}$ . The QD spontaneous-emission lifetime measured in an unpatterned region of the device is  $\tau_{\text{QD}} = 1.4 \text{ ns}$  between 5 K and 100 K (see Supplement 1). Within the PhC cavity, the combination of low cavity mode volume and high  $Q$  factor leads to a significant Purcell enhancement. By comparing dynamical measurements with a microscopic semiconductor model, excellent agreement is

obtained for a cavity-modified lifetime of 305 ps at 300 K, implying a Purcell factor of around five.

An important aspect of our device is the ability to control its emission and photon correlation statistics by temperature-tuning the number of QDs that couple to the laser mode. From 5 K to 300 K, the center of the QD spontaneous emission shifts from 1540 to 1580 nm and the linewidth broadens from  $\sim 20$  nm to  $\sim 100$  nm. Figure 2(a) illustrates how the center of the inhomogeneous ensemble is strongly detuned at low temperatures (black). Feeding into the cavity mode is provided by only a few resonant emitters and is likely aided by off-resonant coupling of detuned background emitters through a quasicontinuum of excitonic transitions due to the complex multi-exciton level structure in the QDs [12–14]. At room temperature, a strong overlap of the emitter ensemble with the cavity mode is observed (red) and, from the theory, we estimate that  $\sim 240$  emitting dipoles efficiently couple to the laser mode.

## B. Input-Output Characteristics

The nanolaser is held in a vacuum in a closed-cycle cryostat with a variable temperature from 4 K to 300 K. Optical excitation is provided by a Ti:sapphire laser emitting 1 ps pulses centered at 805 nm at an 82 MHz repetition rate. A 0.5 numerical-aperture objective is used to focus and collect infrared light from the device. Emitted light is spectrally filtered with 2 nm bandwidth centered at the cavity resonance and then coupled into a single-mode optical fiber.

The input-output device characteristics are shown for different temperatures in Fig. 2(b), with the excitation pulse area and the integrated emission intensity plotted on the horizontal and vertical axes, respectively. At room temperature (red circles), the typical S-shaped curve is indicative of a clear transition from primarily spontaneous emission (LED operation) to lasing, separated by a threshold region that extends over nearly one order of magnitude in excitation power. Such smeared-out threshold behavior is characteristic of cavity-enhanced high  $\beta$ -factor devices from which a large fraction of spontaneous emission is into the lasing mode [15]. Importantly, the integrated output intensity saturates at the highest excitation powers (i.e., the laser mode is fed by a limited number of saturable emitters). By lowering the temperature, the attainable gain is reduced by QDs being tuned out of resonance with the laser mode. At 100 K (blue symbols), the emission intensity saturates already during the threshold, and a threshold appears to be fully absent at 5 K (black symbols). In this case, the gain saturates completely before a sufficient number of intracavity photons are present to initiate lasing. In Section 4 and in Supplement 1, we present photon autocorrelation measurements confirming that at temperatures below  $\approx 75$  K, the device operates in this type of LED regime and behaves as a thermal light source with  $g^{(2)}(t_1, t_1) > 1$  at all times  $t$  during the emission pulse.

To further confirm our claim of a gain-tunable QD nanolaser, we invoke a microscopic semiconductor laser theory that provides access to the full emission and correlation dynamics in a quantum-optical framework. Before the model is introduced in the following section, we interpret the input–output characteristics based on the theoretical results shown as solid lines in Fig. 2(b). Overall excellent agreement is achieved with a single parameter set for the device that is provided in Supplement 1. To accommodate the temperature tuning of the gain, the

involved emitting dipole number is changed from 240 (300 K) to 10 (5 K). Simple rate-equation models relate the jump in the emission intensity at the threshold to the  $\beta$  factor [16]. Here, it is worth noticing that we use a temperature-independent value of  $\beta = 0.04$ . The reduction of the jump when lowering the temperature from 300 K to 100 K might be intuitively attributed to an increased  $\beta$  factor, but is in fact caused by the onset of saturation before the threshold is fully developed [17]. The  $\beta$  factor itself is determined by the ratio of spontaneous emission channels and is therefore not expected to change much with the temperature.

A  $\beta$  factor of 0.04 corresponds to  $\beta^{-1/2} \approx 5$  photons in the cavity at the lasing threshold. A large  $\beta$  factor for nanolasers is in contrast to macroscopic ( $\beta \lesssim 10^{-4}$ ) and mesoscale ( $10^{-4} \lesssim \beta \lesssim 10^{-2}$ ) lasers with significantly more gain material and cavity photons at the threshold [18]. Consequently, in nanolasers the emission and photon statistics are particularly sensitive to large relative fluctuations in the photon number, which scale as  $\approx \beta^{1/4}$  and can be as large as 40% for our device [19]. In QD nanolasers with high  $\beta$  factors similar to that presented here, large fluctuations in the photon number are responsible for strong intensity and timing fluctuations that are correlated, leading to a departure from coherent and Poissonian statistics in the emission dynamics [8,20] that are presented in Section 4. Before discussing the details of these measurements, we first introduce the theory used to access the emission and photon-correlation dynamics.

## 3. THEORETICAL MODEL FOR THE LASER EMISSION AND PHOTON CORRELATION DYNAMICS

The characterization of nanolasers in terms of the statistical properties of the emission (photon correlations) requires a treatment beyond rate-equation approaches. The cluster-expansion method has proven to be a reliable scheme to systematically include carrier and photon correlations and to map out their influence on the dynamical and steady-state properties of semiconductor nanolaser devices [21–24]. Particularly at low temperatures, our device operates deep in the cavity-QED regime, in which few emitters ( $\sim 10$ ) couple to a high- $Q$  cavity mode. In this regime, spontaneous emission plays an important role even at and above the threshold. By using the quantized electromagnetic field, spontaneous emission arises naturally, and dynamical equations for carrier–photon and photon–photon correlation functions give access to the photon autocorrelation function  $g^{(2)}(t_1, t_2)$ .

From the semiconductor Hamiltonian, a set of coupled equations of motion are derived for the mean photon number in the laser mode  $\langle b^\dagger b \rangle$  and the electron and hole fractional populations  $f_s^{e,h}$  in the lasing level of the QDs,

$$\left( \hbar \frac{d}{dt} + 2\kappa \right) \langle b^\dagger b \rangle = 2N|g|^2 \text{Re}[\langle b^\dagger v_s^\dagger c_s \rangle], \quad (2)$$

$$\hbar \frac{d}{dt} f_s^{e,h} = -2|g|^2 \text{Re}[\langle b^\dagger v_s^\dagger c_s \rangle] + \mathcal{R}_{nl}(\beta) + \mathcal{R}_{p \rightarrow s}^{e,h}(P). \quad (3)$$

Here,  $\kappa$  represents the photon escape rate,  $g$  denotes the light–matter coupling constant,  $N$  is the number of emitting dipoles in the cavity, and  $c_s^\dagger (c_s)$  and  $v_s^\dagger (v_s)$  are the creation (annihilation) operators for the carriers in the s-shell conduction- or valence-band state of each QD emitter. The cavity field is addressed by the Bosonic operators  $b$  and  $b^\dagger$ . The quantities  $\mathcal{R}_{p \rightarrow s}$  contain the scattering rates of carrier excitation from energetically higher

p-states into the lasing level of the dots. The spontaneous loss of carriers into nonlasing modes at rate  $\mathcal{R}_{nl}$ , together with  $g$  and the dephasing and cavity-loss rates, implicitly define the  $\beta$  factor that quantifies the ratio of the spontaneous emission in the photonic mode relative to the total spontaneous emission. Details and a derivation are given in Supplement 1.

Both the mean photon number and the carrier population dynamics (2)–(3) are driven by the photon-assisted polarization  $\langle b^\dagger v_s^\dagger c_s \rangle$  that describes an interband transition via the emission of a photon into the laser mode. Its dynamics follows a separate equation of motion,

$$\left( \hbar \frac{d}{dt} + \kappa + \Gamma \right) \langle b^\dagger v_s^\dagger c_s \rangle = f_s^e f_s^h - (1 - f_s^e - f_s^h) \langle b^\dagger b \rangle + \delta \langle b^\dagger b c_s^\dagger c_s \rangle - \delta \langle b^\dagger b v_s^\dagger v_s \rangle, \quad (4)$$

introducing a timescale determined by the balance of gain contributions due to spontaneous emission  $\propto f_s^e f_s^h$ , stimulated contributions  $\propto \langle b^\dagger b \rangle$ , and dissipation due to cavity losses  $\kappa$  and homogeneous dephasing  $\Gamma$ . It is important to note that the dimension of the quantity  $\langle b^\dagger v_s^\dagger c_s \rangle$  is 1/energy (see [21] for more details). Rate equations can be obtained by adiabatically eliminating the dynamics of the photon-assisted polarization while neglecting higher-order carrier–photon correlations that contribute to stimulated emission in the second line [21]; however, the dynamical evolution of these correlations plays a central role in understanding the formation of coherent emission in Section 5.

Accessing the two-time second-order photon correlation function given by Eq. (1) is a two-step process. First, the zero-delay value  $g^{(2)}(t_1, t_1)$  is obtained by augmenting the dynamics of Eqs. (2)–(4) with that of additional carrier–photon correlation functions  $\delta \langle b^\dagger b c_s^\dagger c_s \rangle$ ,  $\delta \langle b^\dagger b v_s^\dagger v_s \rangle$ , and  $\delta \langle b^\dagger b^\dagger b v_s^\dagger c_s \rangle$ . In a second step, the two-time map of  $g^{(2)}(t_1, t_2)$  is obtained by solving a time evolution with respect to the delay-time  $\tau = t_2 - t_1$  at each time step  $t_1$ . Details of this procedure are given in Supplement 1.

#### 4. PHOTON CORRELATION DYNAMICS

Photon correlation dynamics are measured using a modified HBT interferometer that provides access to the full two-time photon correlation function. This approach is similar to a previous study examining single-photon purity from a single QD [25]. A schematic illustration of the setup is shown in Fig. 3. The light emitted from the nanolaser is spectrally filtered, split using a

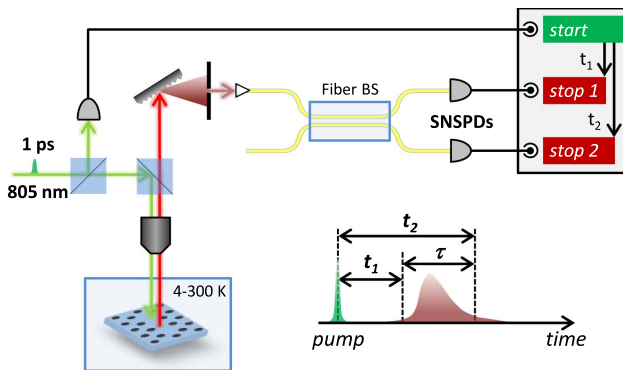


**Fig. 3.** Illustration of the Hanbury Brown and Twiss setup with fiber-coupled superconducting nanowire single photon detectors (SNSPDs) for mapping the dynamics of  $g^{(2)}(t_1, t_2)$ .

fiber-based 50:50 beam splitter (BS), and then measured with WSi superconducting nanowire single-photon detectors (SNSPDs) with a timing jitter of  $\approx 75$  ps full-width at half-maximum (see Supplement 1). Photon arrival times  $t_1$  and  $t_2$  at the two SNSPDs are recorded relative to the Ti:sapphire excitation pulse. The time-tagged data are post-processed to construct dual start-stop correlation histograms that provide a complete mapping in  $t_1$  and  $t_2$  of the second-order photon correlation function  $g^{(2)}(t_1, t_2)$  (see timing diagram in the inset to Fig. 3). Measured and calculated two-time maps of  $g^{(2)}(t_1, t_2)$  are presented in Fig. 4 for the LED (5 K) and lasing (100 K) operational regimes of our device at the highest excitation powers  $P3$ , as indicated by the arrows in Fig. 2(b). The full two-time characteristics as obtained from experiment (top row) and theory (bottom row) are in reasonable agreement which, to the best of our knowledge, has not been presented before.

The  $g^{(2)}(t_1, t_2)$  maps can be interpreted by revisiting Eq. (1). The numerator describes the relative probability of detecting two photons at times  $t_1$  and  $t_2$ . The denominator describes the probability of detecting two photons at  $t_1$  and  $t_2$ , assuming these two photons are uncorrelated with one another (see Supplement 1). Because our source is pulsed, the temporal dynamics of  $g^{(2)}(t_1, t_2)$  do not reduce to a simple single-time dependence on  $\tau = t_2 - t_1$ , as they would for a stationary source [26]. This can be seen by taking a slice along the diagonal line in Fig. 4 for which  $\tau$  is fixed. The diagonal line through the origin shows the dynamics for  $\tau = 0$ .

As an example, at 100 K, see the right panel of Fig. 4(a). If one photon is detected at  $t_1 = 0.1$  ns, then the likelihood of a second photon being detected at  $t_2 = 0.1$  ns (0.5 ns) is higher (lower) than it would be for a coherent state with the same temporal intensity profile. Slices along the diagonal for  $\tau = 0$  are shown (points) together with the emission intensity (solid lines) for the LED and lasing operational regimes of our device in Figs. 5(a) and 5(b). The selected excitation powers  $P1$ ,  $P2$ , and  $P3$  are indicated by the arrows in Fig. 2(b) and, in the case of the device

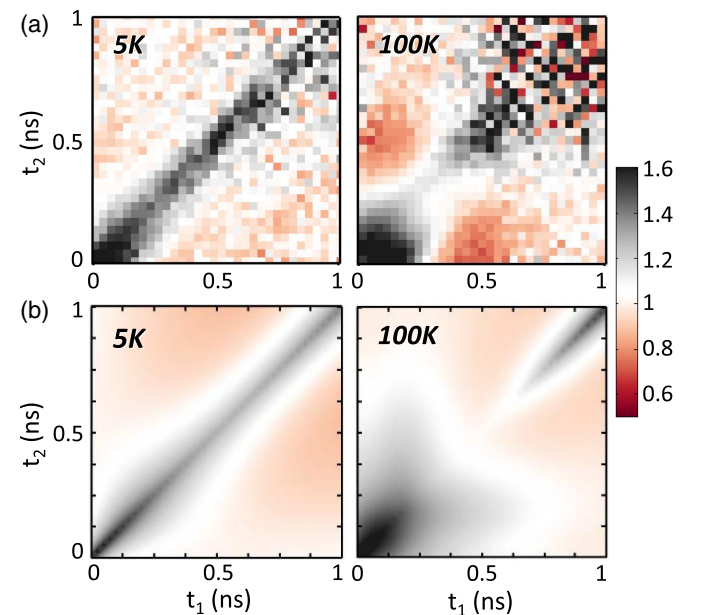


**Fig. 4.** (a) Measured and (b) calculated two-time maps of  $g^{(2)}(t_1, t_2)$  for 5 K (left) and 100 K (right).

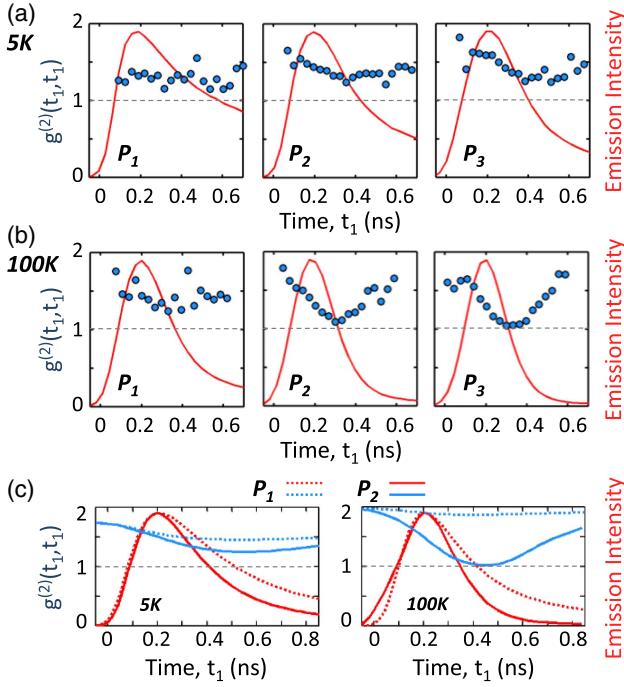


**Fig. 5.** Blue circles: Time-resolved zero-delay autocorrelation function (diagonal cuts of the two-time maps shown in the previous figure for which  $t_1 = t_2$ ). (a) In the LED regime at 5 K,  $g^{(2)}(t_1, t_1) > 1$  as expected for incoherent thermal radiation. These dynamics are in marked contrast to 100 K for which  $g^{(2)}(t_1, t_1)$  reaches unity during emission, which is shown in (b). The emission pulse intensity is indicated by the solid red line for reference. (c) Calculated dynamics.

operating at 100 K, correspond to below, at, and above the threshold. Theoretical results are provided in Fig. 5(c). At 5 K (panel a),  $g^{(2)}(t_1, t_1) > 1$  throughout the entire pulse and does not change significantly with excitation power, as is expected for a thermal light source. Although an ideal value of two is expected for thermal emission, smaller values are observed, possibly due to the temporal resolution of the HBT experiment (see Supplement 1).

At 100 K, sufficient gain leads to the development of a threshold region in the input–output curve in Fig. 2(b). This interpretation is confirmed by the autocorrelation measurements in Fig. 5(b). Below the threshold ( $P_1$ ),  $g^{(2)}(t_1, t_1) > 1$  at all times, whereas a value of one is reached during the emission pulse at higher excitation powers  $P_2, P_3 > 2 \mu\text{W}$ , confirming that the carrier density is high enough to drive coherent emission. It is noteworthy that under pulsed excitation, the emission pulse of a nanolaser undergoes various stages: After carriers have been created by the excitation pulse, the confined QD states that feed the laser transition are filled by carrier scattering on a timescale of the carrier relaxation time  $\tau_r \approx 500$  fs. Already during the relaxation process, spontaneous thermal emission begins as soon as carriers populate the lasing levels (rising edge of the emission pulse). At the peak of the emission pulse at time  $t_{\text{peak}}$ , the photon density in the cavity mode is at its highest value, and one would readily expect coherent emission with  $g^{(2)}(t_{\text{peak}}, t_{\text{peak}}) = 1$  due to stimulated emission. However, a closer examination of the data shown in Fig. 5 reveals a significant temporal delay  $\delta t$  between the maximum of the emission peak and the formation of coherent emission expressed by the minimum in the autocorrelation function.

We find that the delay  $\delta t$  increases from  $\sim 150$  ps to  $\sim 300$  ps with temperature in the measurements and theory, leading to the high-intensity portion of the pulse being largely thermal despite the system operating in the regime of stimulated emission. These dynamics are in marked contrast to a previous study of a QD micropillar laser with  $Q \approx 5,000$ , in which the onset of coherent emission coincides with the onset of stimulated emission at the pulse intensity maximum [27].

## 5. NON-MARKOVIAN DELAY OF SECOND-ORDER COHERENCE IN HIGH-Q NANOLASERS

Since the coupled equations of motion of the microscopic laser model accurately reproduce the observed delay in the formation of coherence, more insight can be obtained from theory. Equations (2)–(4) already show that the photon production does not adiabatically follow its source (namely spontaneous and stimulated emission), but is determined by the photon-assisted polarization that has its own dynamical evolution given by Eq. (4). A similar relationship exists [21] between the higher-order photon-correlation function  $\delta\langle b^\dagger b^\dagger bb \rangle$  that determines  $g^{(2)}(t_1, t_2) = 2 + \delta\langle b^\dagger b^\dagger bb \rangle / \delta\langle b^\dagger b \rangle^2$ , and the higher-order photon-assisted polarization  $\delta\langle b^\dagger b^\dagger b v_s^\dagger c_s \rangle$  that describes interband recombination and the emission of a photon in the presence of an additional photon. This process obeys the time evolution [21],

$$\left( \hbar \frac{d}{dt} \right) \delta\langle b^\dagger b^\dagger b v_s^\dagger c_s \rangle = -(3\kappa + \Gamma) \delta\langle b^\dagger b^\dagger b v_s^\dagger c_s \rangle + 2|g|^2 \langle b^\dagger v_s^\dagger c_s \rangle^2 - (1 - f_s^e - f_s^h) \delta\langle b^\dagger b^\dagger bb \rangle + 2f_s^h \langle b^\dagger b c_s^\dagger c_s \rangle - 2f_s^e \langle b^\dagger b v_s^\dagger v_s \rangle + \langle b^\dagger b \rangle (\delta\langle b^\dagger b c_s^\dagger c_s \rangle - \delta\langle b^\dagger b v_s^\dagger v_s \rangle). \quad (5)$$

An understanding of the origin of delayed coherence formation can be obtained by identifying the dominant contributions to the time evolution of both polarizations, Eqs. (4) and (5), at the onset of lasing, given by the terms  $\propto \langle b^\dagger b \rangle$ . While the time evolution of the photon production follows the polarization via the carrier inversion term  $(1 - f_s^e - f_s^h)$ , the evolution of the higher-order polarization is driven by correlations between carriers and photons  $(\delta\langle b^\dagger b c_s^\dagger c_s \rangle - \delta\langle b^\dagger b v_s^\dagger v_s \rangle)$ . These carrier–photon correlations obey their own time evolution, which differs from that of the carrier populations,

$$\left( \hbar \frac{d}{dt} + 2\kappa \right) \langle b^\dagger b c_s^\dagger c_s \rangle = -2|g|^2 [\delta\langle b^\dagger b^\dagger b v_s^\dagger c_s \rangle + (\langle b^\dagger b \rangle + f_s^e) \langle b^\dagger v_s^\dagger c_s \rangle], \quad (6)$$

$$\left( \hbar \frac{d}{dt} + 2\kappa \right) \langle b^\dagger b v_s^\dagger v_s \rangle = 2|g|^2 [\delta\langle b^\dagger b^\dagger b v_s^\dagger c_s \rangle + (\langle b^\dagger b \rangle + f_s^h) \langle b^\dagger v_s^\dagger c_s \rangle]. \quad (7)$$

To pin down the responsible factor for the delay, we eliminate the dynamics of the carrier–photon correlations by solving Eqs. (6) and (7) adiabatically.

In Fig. 6, the dynamics of the remaining equations of motion (blue dashed curve) are compared to the full dynamics (blue solid curve). Evidently, when the correlation dynamics are eliminated in a Markovian sense, the delay disappears and the maximum of the emission peak coincides with the minimum of the autocorrelation function.

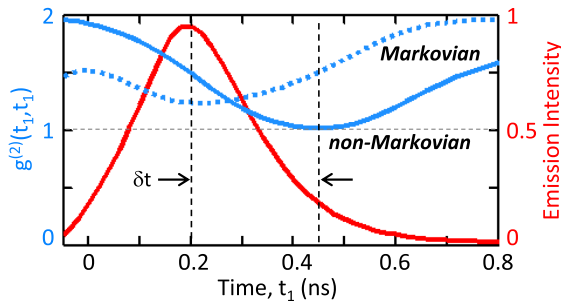


**Fig. 6.** Comparison of the correlation dynamics from the full set of coupled laser equations (solid blue curve) and dynamics in which the correlations between carriers and photons are adiabatically eliminated (dashed blue curve). The disappearance of the delay  $\delta t$  in the formation of coherence in the latter case identifies the non-Markovian polarization dynamics as the origin of the observed effect.

relation function (blue dashed curve). Therefore, this confirms our initial assertion that the traditional lasing picture, in which coherent emission is directly related to the presence of stimulated emission, is too simple. Instead, the photon number and its fluctuations respond to microscopic polarizations, and these develop on different timescales due to the presence of carrier–photon correlations, causing the observed effect.

Finally, we identify the delay in coherence formation as a property of high- $Q$  nanolasers that is generally absent in conventional laser devices. In Fig. 7, the delay  $\delta t$  is plotted against the cavity- $Q$  factor for three different sets of parameters that are representative of typical laser systems and, in particular, the number  $N$  of involved emitting dipoles. As a general trend, a delay begins to form for  $Q$ -factors above 10,000 and can, in principle, become as large as 0.5 ns in cavities with extreme  $Q$  factors, such as microsphere or whispering-gallery mode resonators [28]. Lower- $Q$  cavities require a larger amount of gain material to cross the threshold, which is why the curves for 20, 75, and 240 emitters set in at a minimum  $Q$ -value. Below this value, stimulated emission is not reached, and the system operates as an LED. In the bad-cavity regime, lasing can be reached with sufficient gain material and the absence of a delay. Then, a Markovian description of the laser dynamics, in which coherence forms as an instantaneous response of the photonic field to stimulated emission, is justified.

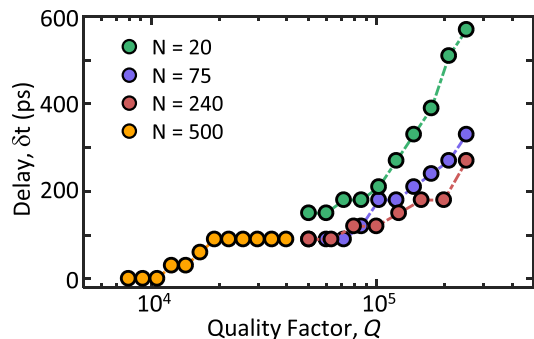


**Fig. 7.** Delay  $\delta t$  between emission intensity maximum and the minimum in the zero-delay second-order photon autocorrelation function as a function of the cavity- $Q$  factor. The results are obtained for  $g$ ,  $\kappa$ , and  $\beta$  as given in the Supplement 1. A dephasing rate of  $\Gamma = 0.5$  meV (0.7 meV) is used for  $N = 20$  and 75 (240 and 500). Note that a few-emitter gain material requires a sufficiently high cavity- $Q$  factor to reach lasing. Below that,  $g^{(2)}$  remains thermal and an offset  $\delta t$  can no longer be defined.

## 6. SUMMARY

A QD-PhC nanolaser has been demonstrated to operate in regimes of LED and laser emission by temperature-tuning the amount of gain material that couples to the laser mode. Photon correlation spectroscopy with high temporal resolution and microscopic laser theory have been combined to reveal a non-instantaneous response of the photon-autocorrelation function to the onset of stimulated emission. As a result, the emission pulse of our nanolaser is largely thermal and becomes coherent with a delay of 250 ps after the emission-pulse maximum has been reached at the peak of stimulated emission. The origin of this effect lies in the non-Markovian dynamics of microscopic polarization that is the response of the gain material to spontaneous and stimulated emission. While the effect plays no role in the bad-cavity regime of conventional lasers, it is of central importance in the design of cavity-QED enhanced nanolasers that operate with little gain material in high- $Q$  cavities with  $Q \gtrsim 10^4$ . This new dynamical effect should stimulate further investigations into the modulation response of such devices.

**Funding.** Deutsche Forschungsgemeinschaft (Dfg).

See Supplement 1 for supporting content.

## REFERENCES

1. I. Prieto, J. M. Llorens, L. E. Munoz-Camunez, A. G. Taboada, J. Canet-Ferrer, J. M. Ripalda, C. Robles, G. Munoz-Matutano, J. P. Martinez-Pastor, and P. A. Postigo, "Near thresholdless laser operation at room temperature," *Optica* **2**, 66–69 (2015).
2. E. M. Purcell, "Spontaneous emission probability at radio frequencies," *Phys. Rev.* **69**, 681 (1946).
3. H. Altug, D. Englund, and J. Vučković, "Ultrafast photonic crystal nanocavity laser," *Nat. Phys.* **2**, 484–488 (2006).
4. G. T. Noe II, J.-H. Kim, J. Lee, Y. Wang, A. K. Wójcik, S. A. McGill, D. H. Reitze, A. A. Belyanin, and J. Kono, "Giant superfluorescent bursts from a semiconductor magneto-plasma," *Nat. Phys.* **8**, 219–224 (2012).
5. F. Jahnke, C. Gies, M. Aßmann, M. Bayer, H. A. M. Leymann, A. Foerster, J. Wiersig, C. Schneider, M. Kamp, and S. Höfling, "Giant photon bunching, superradiant pulse emission and excitation trapping in quantum-dot nanolasers," *Nat. Commun.* **7**, 11540 (2016).
6. P. Tighineanu, R. S. Daveau, T. B. Lehmann, H. E. Beere, D. A. Ritchie, P. Lodahl, and S. Stobbe, "Single-photon superradiance from a quantum dot," *Phys. Rev. Lett.* **116**, 163604 (2016).
7. M. Nomura, N. Kumagai, S. Iwamoto, Y. Ota, and Y. Arakawa, "Laser oscillation in a strongly coupled single-quantum-dot-nanocavity system," *Nat. Phys.* **6**, 279–283 (2010).
8. A. Lebreton, I. Abram, R. Braive, N. Belabas, I. Sagnes, F. Marsili, V. B. Verma, S. W. Nam, T. Gerrits, I. Robert-Philip, M. J. Stevens, and A. Beveratos, "Pulse-to-pulse jitter measurement by photon correlation in high-beta lasers," *Appl. Phys. Lett.* **106**, 031108 (2015).
9. W. W. Chow, F. Jahnke, and C. Gies, "Emission properties of nanolasers during the transition to lasing," *Light Sci. Appl.* **3**, e201 (2014).
10. A. Michon, R. Hostein, G. Patriarche, N. Gogneau, G. Beaudoin, A. Beveratos, S. Robert-Philip, S. Sauvage, P. Boucaud, and I. Sagnes, "Metal organic vapor phase epitaxy of InAsP/InP(001) quantum dots for 1.55  $\mu\text{m}$  applications: growth, structural, and optical properties," *J. Appl. Phys.* **104**, 043504 (2008).
11. R. Hostein, A. Michon, G. Beaudoin, N. Gogneau, G. Patriarche, J.-Y. Marzin, I. Robert-Philip, I. Sagnes, and A. Beveratos, "Time-resolved characterization of InAsP/InP quantum dots emitting in the C-band telecommunications window," *Appl. Phys. Lett.* **93**, 073106 (2008).
12. M. Winger, T. Volz, G. Tarel, S. Portolan, A. Badolato, K. J. Hennessy, E. L. Hu, A. Beveratos, J. Finley, V. Savona, and A. Imamoglu,

- "Explanation of photon correlation in the far-off-resonance optical emission from a quantum-dot-cavity system," *Phys. Rev. Lett.* **103**, 207403 (2009).
13. D. Elvira, R. Hostein, B. Fain, L. Monniello, A. Michon, G. Beaudoin, R. Braive, I. Robert-Philip, I. Abram, I. Sagnes, and A. Beveratos, "Single InAsP/InP quantum dots as telecommunications-band photon sources," *Phys. Rev. B* **84**, 195302 (2011).
  14. S. Lichtmannecker, M. Florian, T. Reichert, M. Blauth, M. Bichler, F. Jahnke, J. J. Finley, C. Gies, and M. Kaniber, "A few-emitter solid-state multi-exciton laser," *Sci. Rep.* **7**, 7420 (2017).
  15. S. M. Ulrich, C. Gies, S. Ates, J. Wiersig, S. Reitzenstein, C. Hofmann, A. Löffler, A. Forchel, F. Jahnke, and P. Michler, "Photon statistics of semiconductor microcavity lasers," *Phys. Rev. Lett.* **98**, 043906 (2007).
  16. H. Yokoyama and S. D. Brorson, "Rate equation analysis of microcavity lasers," *J. Appl. Phys.* **66**, 4801–4805 (1989).
  17. C. Gies, J. Wiersig, and F. Jahnke, "Output characteristics of pulsed and continuous-wave-excited quantum-dot microcavity lasers," *Phys. Rev. Lett.* **101**, 067401 (2008).
  18. T. Wang, G. P. Puccioni, and G. L. Lippi, "How mesoscale lasers can answer fundamental questions related to nanolasers," *Proc. SPIE* **9884**, 98840B (2016).
  19. P. A. Rice and H. J. Carmichael, "Photon statistics of a cavity-QED laser: a comment on the laser-phase-transition analogy," *Phys. Rev. A* **50**, 4318–4329 (1994).
  20. D. Elvira, X. Hachair, V. B. Verma, R. Braive, G. Beaudoin, I. Robert-Philip, I. Sagnes, B. Baek, S. W. Nam, E. A. Dauler, I. Abram, M. J. Stevens, and A. Beveratos, "Higher-order photon correlation in pulsed photonic crystal nanolasers," *Phys. Rev. A* **84**, 061802 (2011).
  21. C. Gies, J. Wiersig, M. Lorke, and F. Jahnke, "Semiconductor model for quantum-dot-based microcavity lasers," *Phys. Rev. A* **75**, 013803 (2007).
  22. M. Kira and S. W. Koch, *Semiconductor Quantum Optics* (Cambridge University, 2011).
  23. A. Carmele, A. Knorr, and M. Richter, "Photon statistics as a probe for exciton correlations in coupled nanostructures," *Phys. Rev. B* **79**, 035316 (2009).
  24. H. A. M. Leymann, A. Foerster, and J. Wiersig, "Expectation value based equation-of-motion approach for open quantum systems: a general formalism," *Phys. Rev. B* **89**, 085308 (2014).
  25. E. B. Flagg, S. V. Polyakov, T. Thomay, and G. S. Solomon, "Dynamics of nonclassical light from a single solid-state quantum emitter," *Phys. Rev. Lett.* **109**, 163601 (2012).
  26. J. Wiersig, C. Gies, F. Jahnke, M. Assman, T. Berstermann, M. Bayer, C. Kistner, S. Reitzenstein, C. Schneider, S. Hofling, A. Forchel, C. Kruse, J. Kalden, and D. Hommel, "Direct observation of correlations between individual photon emission events of a microcavity laser," *Nature* **460**, 245–249 (2009).
  27. M. Aßmann, F. Veit, M. Bayer, C. Gies, F. Jahnke, S. Reitzenstein, S. Hofling, L. Worschech, and A. Forchel, "Ultrafast tracking of second-order photon correlation in the emission of quantum-dot microresonator lasers," *Phys. Rev. B* **81**, 165314 (2010).
  28. D. K. Armani, T. J. Kippenberg, S. M. Spillane, and K. J. Vahala, "Ultra-high-Q toroid microcavity on a chip," *Nature* **421**, 925–928 (2003).